Supporting Information

Direct Band Gap Chalcohalide Semiconductors: Quaternary $AgBiSCl_2$ Nanocrystals

Danila Quarta,[a†] Stefano Toso,[b,c†] Antonio Fieramosca,[a] Lorenzo Dominici,[a] Rocco Caliandro,[c] Anna Moliterni,[c] David Maria Tobaldi,[a] Gabriele Saleh,[b] Irina Gushchina,[b] Rosaria Brescia,[b] Mirko Prato,[b] Ivan Infante,[b,d,e] Adriano Cola,[f] Cinzia Giannini,[c] Liberato Manna,[b] Giuseppe Gigli,[a,g] Carlo Giansante[a]**

[a] *Consiglio Nazionale delle Ricerche, Istituto di Nanotecnologia − CNR NANOTEC, Via Monteroni, 73100 Lecce − Italy*

[b] *Istituto Italiano di Tecnologia − IIT, Via Morego 30, 16163 Genova − Italy*

[c] *Consiglio Nazionale delle Ricerche, Istituto di Cristallografia − CNR IC, Via Amendola 122/o, 70126 Bari – Italy*

[d] *BCMaterials, Basque Center for Materials, Applications, and Nanostructures, UPV/EHU Science Park, Leioa 48940 – Spain*

[e] *Ikerbasque, Basque Foundation for Science, Bilbao 48009 – Spain*

[f] *Consiglio Nazionale delle Ricerche, Istituto di Microelettronica e Microsistemi − CNR IMM, Via Monteroni, 73100 Lecce − Italy*

[g] *Dipartimento di Fisica, Unisalento, Via per Arnesano, 73100 Lecce − Italy*

[†] equal contribution

* e-mail: anna.moliterni@cnr.it; carlo.giansante@nanotec.cnr.it

Structural Characterization by Synchrotron X-Ray Powder Diffraction (XPD) and Pair Distribution Function (PDF).

To verify the phase purity of the NC compound, the synchrotron XPD profile was first used to carry out a qualitative phase analysis *via* the software *QUALX2.0*[S1], searching for the best-matching crystal phase, among the known single phase diffraction patterns stored in the POW_COD[S1] database (built from COD)[S2]. The phase analysis confirmed the purity of the $AgBiSCl_2$ NC powders and identified the most plausible candidate phase, *i.e*., the POW_COD entry n. 00-150-9232, referred to a crystal structure solved by single crystal diffraction data (published unit cell and space group: *a*=3.971 Å, *b*=13.712 Å, *c*=8.824 Å; V= 480.47 $Å^3$; *Cmcm*)[S3] and stored in the ICSD and CCDC database with the code n. 413290 and 1728322, respectively.

Ab-initio structure solution from synchrotron XPD data.

All the steps of the *ab-initio* structure solution process (*i.e*., indexing, space group determination, full pattern decomposition, structure solution and structure model optimization) were carried out by *EXPO2014*.[S4] During the first step, 46 peak positions, lying in the 1.5°-11.80° 2θ range, were provided to the indexing program *N-TREOR09*[S5], implemented in *EXPO2014*, that identified an orthorhombic cell (cell parameters: *a*=3.9503(11) Å, *b*=13.545(5) Å, *c*=8.778(4) Å; V= 469.7(3) $Å^3$), similar to the literature one[S3] and characterized by a value of the M_{20} de Wolff figure of merit[S6] equal to 19 and no unindexed lines. The next step, *i.e*., the space group determination process, was carried out by exploiting the information on the cell parameters, on the expected cell atomic content and on the integrated intensities extracted in *Pmmm*, *i.e*., the space group with the largest Laue symmetry compatible with the orthorhombic system and no extinction conditions, to search for the presence of systematic absences and to calculate a probability value for the 111 extinction symbols relative to the orthorhombic system[S7]. The automatic approach correctly identified the most probable extinction group (*i.e*., *C− c−*); the related space group *Cmcm* was graphically selected for performing the remaining steps. At the end of the full pattern decomposition procedure, the integrated intensities were processed by Direct Methods[S8] that determined twenty sets of phases, automatically explored by *EXPO2014* providing twenty structure models ranked according to increasing R_F values (R_F is the agreement factor between the calculated and observed structure factor moduli). The most plausible structure model (*i.e*, that one with the lowest R_F value) was selected by *EXPO2014* and revealed itself correctly positioned; in fact, it was in overlap with the literature crystal structure,[S3] with a root mean square deviation RMSD of 0.126 Å, where $RMSD=sqrt(\Sigma_i d_i^2/N_{au})$ is the square root of the averaged squared distances $\{d_i\}$ involving the *i-th* couples of corresponding atoms in the two compared structure models; N_{au}, equal to 4, is the number of atoms in the asymmetric unit of $AgBiSCl_2$. The selected crystal structure was preliminary refined by the Rietveld[S9] procedure implemented in *EXPO2014*, and, if compared with the published one, the corresponding RMSD value lowered to 0.073 Å. The structural model was further improved by using the software Fullprof.[S10]. FullProf Rietveld refinement was carried out by describing the peak shape by a Thompson-Cox-Hastings pseudo-Voigt function and by refining

scale factor, multiple point linear interpolation background, unit cell parameters, anisotropic crystallite size (spherical harmonics), atomic fractional coordinates and isotropic thermal factors. The instrumental resolution function was determined by fitting the XPD data collected for the LaB_6 standard.

Structure refinement from PDF data.

The crystal structure, determined *ab-initio* from synchrotron XPD data, was validated by PDF refinement. It was executed by PDFGUI[S11] for interatomic distances above 2.0 Å, to avoid finite-size artifacts in the low r range. In the first refinement step the following parameters were refined separately (*i.e*. by keeping constant all the remaining ones): the scale factor, lattice parameters, peak shape parameters Q_{broad} (peak broadening from increased intensity noise at high Q) and δ1 (coefficient for 1/r contribution to the peak sharpening) parameters. In the second refinement step, the particle diameter parameter $SP_{diameter}$, describing the PDF shape damping function, and the anisotropic atomic displacement parameters were included in the refinement; the atomic position parameters were refined in the last step.

The main refinement results by PDF and XPD data are reported in Tables S1 and S2, respectively.

Table S1. Main refinement results using PDF data. R_w is the weighted agreement factor between observed and calculated PDF, δ1 is the coefficient for 1/*r* contribution to the peak sharpening, Q_{broad} describes the peak broadening from increased intensity noise at high *Q*.

	$AgBiSCl_2$
R_w	0.121
δ1	1.258
Q_{broad}	0.012
a, *b*, *c* (Å)	3.944, 13.524, 8.775

Table S2. Main refinement results using XPD data. Figures of merit at the end of the Rietveld refinement by FullProf: R_p is the agreement factor between observed and calculated profile, R_{wp} is the weighted-profile reliability parameter, and χ^2 is the Chi-square.

	$AgBiSCl_2$
R_p (%)	7.91
R_{wp} (%)	9.05
χ^2 *	0.1171
a, *b*, *c* (Å)	3.954 (8), 13.55 (3), 8.791 (17)
crystallite size (nm)	55 [100] x 23 [010] x 19 [001]

* the low value of χ^2 is related to the used experimental pattern obtained by averaging the profiles extracted from five diffraction images.

The structural details of the Rietveld refinement by FullProf, provided in Table S3, were similar to the literature ones.[S3] The Ag atoms formed distorted edge- and corner-sharing octahedra with Cl atoms at four vertices (*i.e.*, one Cl atom of the asymmetric unit + three symmetry-equivalent atoms) and S atoms at the two remaining vertices (*i.e.*, one S atom of the asymmetric unit + one symmetry-equivalent atom). As in the case of the published structure,[S3] the distorted octahedra were characterized by two short Ag—S bonds (*i.e.*, bond distance Ag—S= 2.457 (8) Å, see Table S3) and four longer Ag—Cl bonds (*i.e.*, bond distance Ag—Cl= 2.917 (9) Å, see Table S3). Bi atoms were instead bonded in an eight-coordinate geometry (see Figure S1) to six Cl atoms (*i.e.*, one Cl atom of the asymmetric unit + five symmetry-equivalent atoms; Bi—Cl bond lengths ranging from 2.865 (11) Å up 3.163 (8) Å, see Table S3) and two S atoms (*i.e.*, one S atom of the asymmetric unit + one symmetry-equivalent atom; bond distance Bi—S= 2.640 (10) Å, see Table S3).

Table S3. Final fractional atomic coordinates, isotropic displacement parameters (Å^2) and geometric parameters (Å, °) for $AgBiSCl_2$.

	x	*y*	*z*	B_{iso}
Bi1	1.000000	0.29016 (18)	0.750000	2.13972
Ag1	0.500000	0.500000	1.000000	3.44827
Cl1	1.000000	0.3472 (7)	1.0638 (10)	2.55257
S2	0.500000	0.4190 (10)	0.750000	1.54903

Geometric parameters (Å, º)			
Bi1—Cl1	2.865 (11)	Ag1—Cl1	2.917 (9)
Bi1—Cl1^{i}	2.865 (11)	Ag1—S2	2.457 (8)
Bi1—Cl1^{ii}	3.163 (8)	Ag1—S2^{vii}	2.457 (8)
Bi1—Cl1^{iii}	3.163 (8)	Cl1—Bi1^{viii}	3.163 (8)
Bi1—Cl1^{iv}	3.163 (8)	Cl1—Bi1^{ix}	3.163 (8)
Bi1—Cl1^{v}	3.163 (8)	S2—Bi1^{x}	2.640 (10)
Bi1—S2	2.640 (10)	S2—Ag1^{xi}	2.457 (8)
Bi1—S2^{vi}	2.640 (10)		
Cl1—Bi1—Cl1^{i}	148.7 (3)	Cl1^{iii}—Bi1—Cl1^{v}	62.2 (2)
Cl1—Bi1—Cl1^{ii}	131.11 (18)	Cl1^{iii}—Bi1—S2	148.87 (16)
Cl1—Bi1—Cl1^{iii}	131.11 (18)	Cl1^{iii}—Bi1—S2^{vi}	85.20 (19)
Cl1—Bi1—Cl1^{iv}	70.2 (2)	Cl1^{iv}—Bi1—Cl1^{v}	77.35 (16)
Cl1—Bi1—Cl1^{v}	70.2 (2)	Cl1^{iv}—Bi1—S2	85.20 (19)
Cl1—Bi1—S2	79.71 (14)	Cl1^{iv}—Bi1—S2^{vi}	148.87 (16)
Cl1—Bi1—S2^{vi}	79.71 (14)	Cl1^{v}—Bi1—S2	148.87 (16)
Bi1—Cl1—Ag1	90.4 (2)	Cl1^{v}—Bi1—S2^{vi}	85.20 (19)
Bi1—Cl1—Bi1^{viii}	109.8 (3)	S2—Bi1—S2^{vi}	97.0 (2)
Bi1—Cl1—Bi1^{ix}	109.8 (3)	Bi1—S2—Ag1	107.20 (12)
Cl1^{i}—Bi1—Cl1^{ii}	70.2 (2)	Bi1—S2—Bi1^{x}	97.0 (2)

Cl1^{i}—Bi1—Cl1^{iii}	70.2 (2)	Bi1—S2—Ag1^{xi}	107.21
Cl1^{i}—Bi1—Cl1^{iv}	131.11 (18)	Cl1—Ag1—S2	81.7 (3)
Cl1^{i}—Bi1—Cl1^{v}	131.11 (18)	Cl1—Ag1—S2^{vii}	98.82
Cl1^{i}—Bi1—S2	79.71 (14)	Ag1—Cl1—Bi1^{viii}	95.16
Cl1^{i}—Bi1—S2^{vi}	79.71 (14)	Ag1—Cl1—Bi1^{ix}	158.84
Cl1^{ii}—Bi1—Cl1^{iii}	77.35 (16)	S2—Ag1—S2^{vii}	180.00
Cl1^{ii}—Bi1—Cl1^{iv}	62.2 (2)	Ag1—S2—Bi1^{x}	107.21
Cl1^{ii}—Bi1—Cl1^{v}	108.1 (3)	Ag1—S2—Ag1^{xi}	126.98
Cl1^{ii}—Bi1—S2	85.20 (19)	Bi1^{viii}—Cl1—Bi1^{ix}	77.35 (15)
Cl1^{ii}—Bi1—S2^{vi}	148.87 (16)	Bi1^{x}—S2—Ag1^{xi}	107.21
Cl1^{iii}—Bi1—Cl1^{iv}	108.1 (3)		
Cl1^{i}—Bi1—Cl1—Ag1	42.39	Cl1^{ii}—Bi1—S2—Ag1	142.14
Cl1^{i}—Bi1—Cl1—Bi1^{viii}	138.49 (17)	Cl1^{ii}—Bi1—S2—Bi1^{x}	31.19 (15)
Cl1^{i}—Bi1—Cl1—Bi1^{ix}	-138.49 (17)	Cl1^{ii}—Bi1—S2—Ag1^{xi}	-78.82
Cl1^{ii}—Bi1—Cl1—Ag1	-81.57	Cl1^{iii}—Bi1—S2—Ag1	-161.67
Cl1^{ii}—Bi1—Cl1—Bi1^{viii}	14.2 (4)	Cl1^{iii}—Bi1—S2—Bi1^{x}	87.0 (5)
Cl1^{ii}—Bi1—Cl1—Bi1^{ix}	97.2 (2)	Cl1^{iii}—Bi1—S2—Ag1^{xi}	-22.63
Cl1^{iii}—Bi1—Cl1—Ag1	166.35	Cl1^{iv}—Bi1—S2—Ag1	78.82
Cl1^{iii}—Bi1—Cl1—Bi1^{viii}	-97.2 (2)	Cl1^{iv}—Bi1—S2—Bi1^{x}	-31.19 (15)
Cl1^{iii}—Bi1—Cl1—Bi1^{ix}	-14.2 (4)	Cl1^{iv}—Bi1—S2—Ag1^{xi}	-142.14
Cl1^{iv}—Bi1—Cl1—Ag1	-95.73	Cl1^{v}—Bi1—S2—Ag1	22.63
Cl1^{iv}—Bi1—Cl1—Bi1^{viii}	0.0 (3)	Cl1^{v}—Bi1—S2—Bi1^{x}	-87.0 (5)
Cl1^{iv}—Bi1—Cl1—Bi1^{ix}	83.0 (2)	Cl1^{v}—Bi1—S2—Ag1^{xi}	161.67
Cl1^{v}—Bi1—Cl1—Ag1	-179.48	S2^{vi}—Bi1—S2—Ag1	-69.52
Cl1^{v}—Bi1—Cl1—Bi1^{viii}	-83.0 (2)	S2^{vi}—Bi1—S2—Bi1^{x}	180.0 (3)
Cl1^{v}—Bi1—Cl1—Bi1^{ix}	0.0 (3)	S2^{vi}—Bi1—S2—Ag1^{xi}	69.52
S2—Bi1—Cl1—Ag1	-7.11	S2—Ag1—Cl1—Bi1	7.62
S2—Bi1—Cl1—Bi1^{viii}	88.6 (3)	S2—Ag1—Cl1—Bi1^{viii}	-103.11
S2—Bi1—Cl1—Bi1^{ix}	171.9 (3)	S2—Ag1—Cl1—Bi1^{ix}	-169.4 (7)
S2^{vi}—Bi1—Cl1—Ag1	91.89	S2^{vii}—Ag1—Cl1—Bi1	-172.38
S2^{vi}—Bi1—Cl1—Bi1^{viii}	-171.9 (3)	S2^{vii}—Ag1—Cl1—Bi1^{viii}	76.89
S2^{vi}—Bi1—Cl1—Bi1^{ix}	-88.6 (3)	S2^{vii}—Ag1—Cl1—Bi1^{ix}	10.6 (7)
Cl1—Bi1—S2—Ag1	8.90	Cl1—Ag1—S2—Bi1	-8.59
Cl1—Bi1—S2—Bi1^{x}	-101.86 (15)	Cl1—Ag1—S2—Bi1^{x}	94.63
Cl1—Bi1—S2—Ag1^{xi}	147.94	Cl1—Ag1—S2—Ag1^{xi}	-136.98
Cl1^{i}—Bi1—S2—Ag1	-147.94	S2^{vii}—Ag1—S2—Bi1	0.00
Cl1^{i}—Bi1—S2—Bi1^{x}	101.86 (15)	S2^{vii}—Ag1—S2—Bi1^{x}	0.00
Cl1^{i}—Bi1—S2—Ag1^{xi}	-8.90	S2^{vii}—Ag1—S2—Ag1^{xi}	0.00

Symmetry codes: (i) -*x*+2, *y*, -*z*+3/2; (ii) -*x*+3/2, -*y*+1/2, *z*-1/2; (iii) -*x*+5/2, -*y*+1/2, *z*-1/2; (iv) *x*-1/2, -*y*+1/2, -*z*+2; (v) *x*+1/2, -*y*+1/2, -*z*+2; (vi) *x*+1, *y*, *z*; (vii) -*x*+1, -*y*+1, *z*+1/2; (viii) -*x*+3/2, -*y*+1/2, *z*+1/2; (ix) -*x*+5/2, -*y*+1/2, *z*+1/2; (x) *x*-1, *y*, *z*; (xi) -*x*+1, -*y*+1, *z*-1/2.

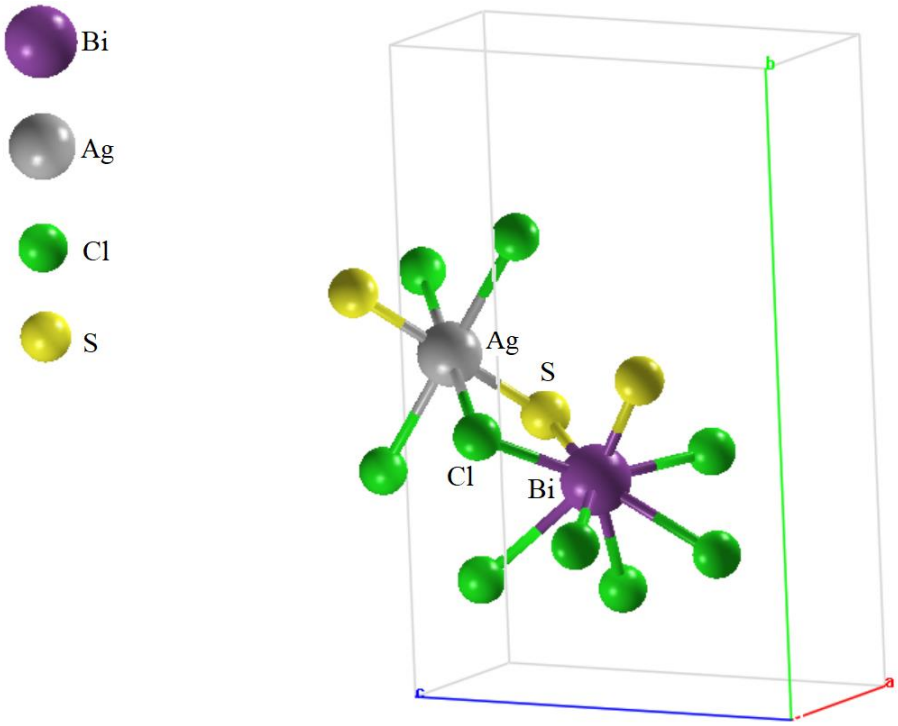

Figure S1. $AgBiSCl_2$: a view of the asymmetric unit (*i.e.*, the four labelled atoms) and its local environment showing the coordination of Bi and Ag atoms at the end of the Rietveld refinement by FullProf.

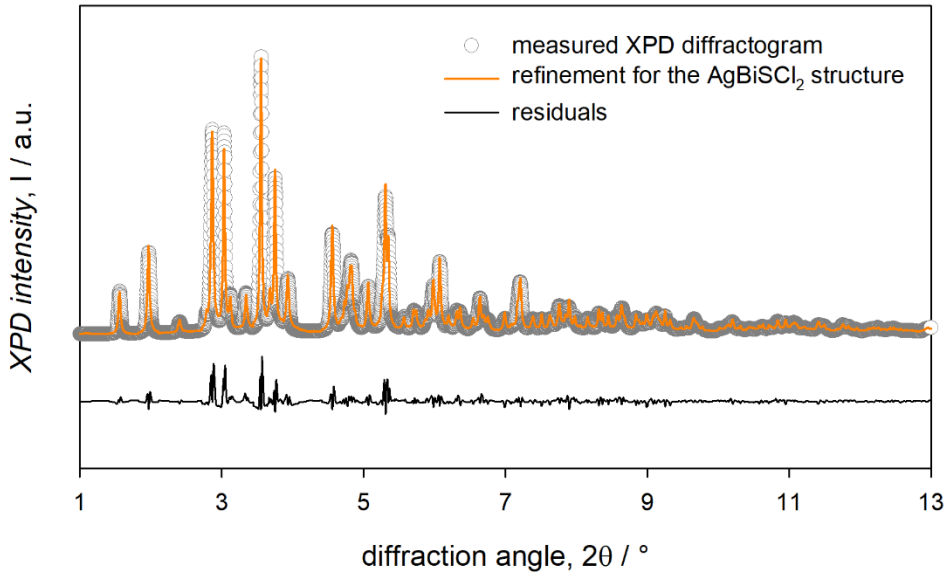

Figure S2. Rietveld refinement of the acquired XPD pattern of the as-synthesized colloidal NCs using the $AgBiSCl_2$ model before the conversion of the 2θ values to emulate the $CuK\alpha_1$ radiation.

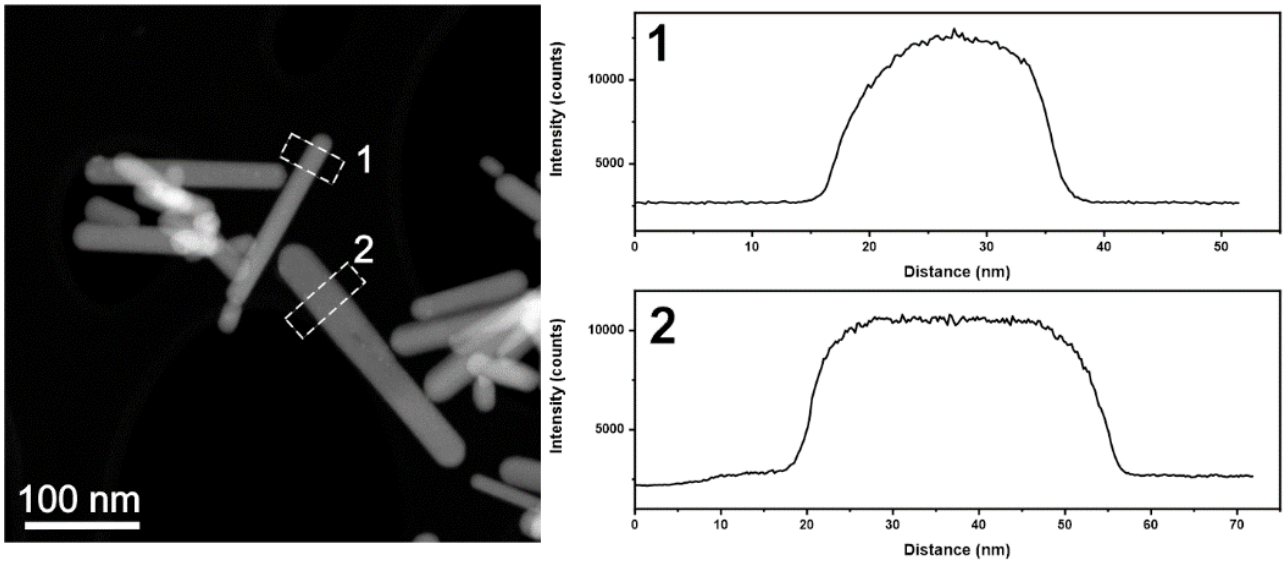

Figure S3. (Left) HAADF-STEM image of a group of $AgBiSCl_2$ NCs, with (right) intensity profiles across two exemplary NCs. The profile over one of the NCs (2) is flat, indicating a homogeneous thickness, while another NC (1) shows a variable intensity, thus thickness. These two types of profiles, exhibited by several NCs, agree with a nanoplatelet-like morphology, with those nanoplatelets lying in some cases flat and in other cases standing on the carbon support film.

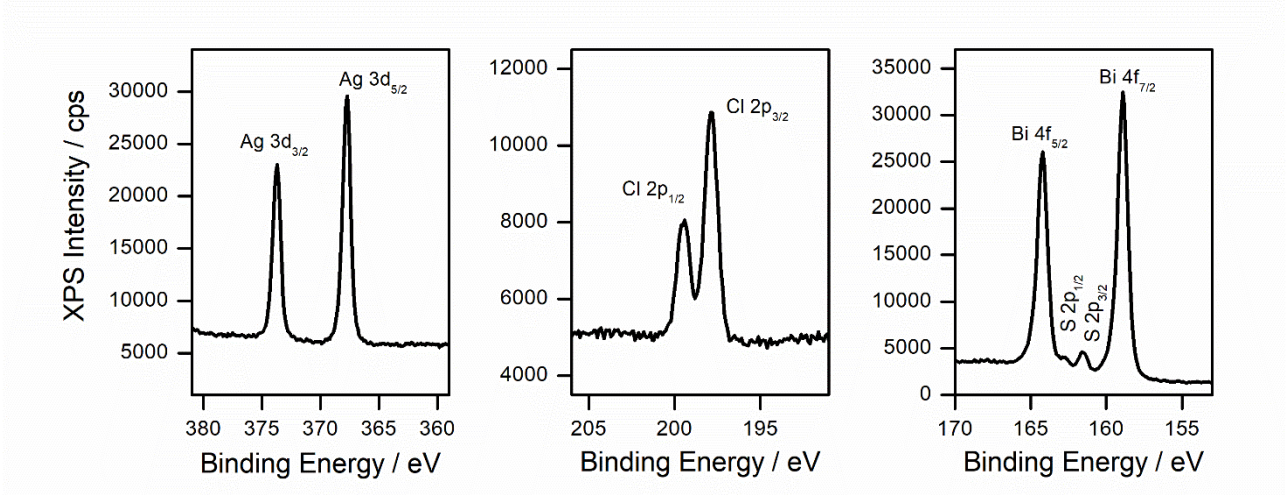

Figure S4. High-resolution XPS spectra showing details of the Ag 3d (left), of the Cl 2p region (center), and Bi 4f and S 2p region (right). The areas of the peaks were used to estimate the relative concentrations of the elements composing the $AgBiSCl_2$ NCs.

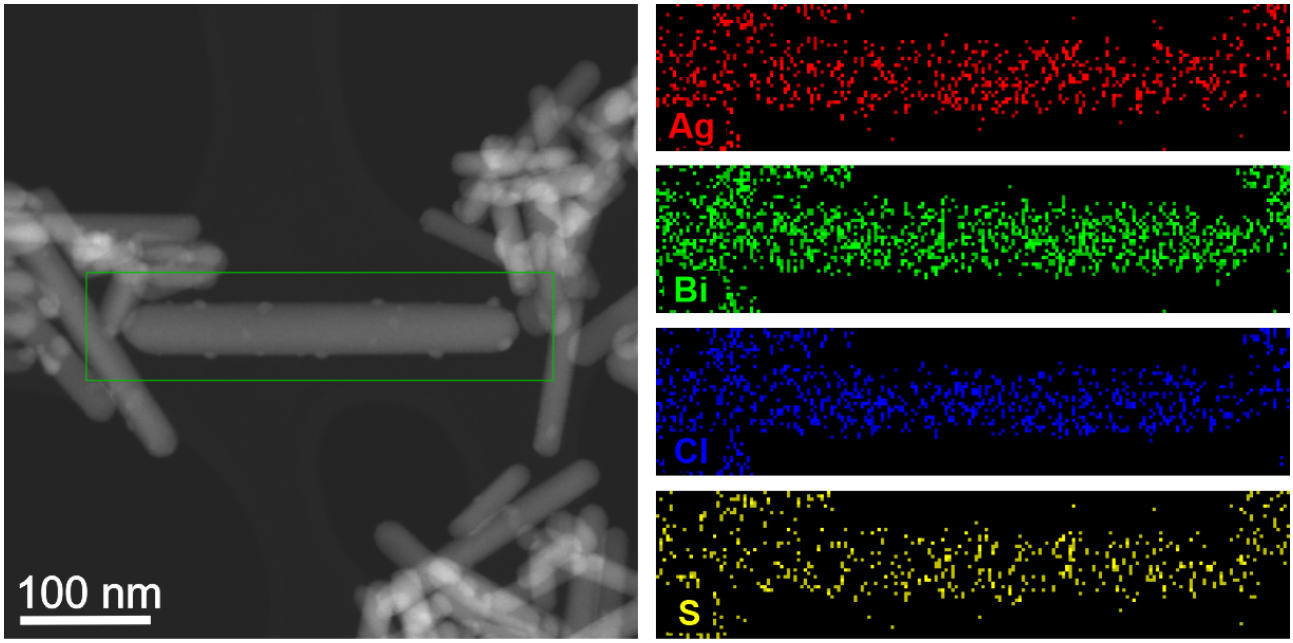

Figure S5. (Left) HAADF-STEM image of a group of NCs and (right) STEM-EDS elemental maps over the NC within the frame. The STEM-EDS maps shown here were obtained by "quantitative mapping", i.e. integrating the net intensities for the S Kα (2.31 keV), Cl Kα (2.62 keV), Bi Lα (10.84 keV) and Ag Lα (2.98 keV) peaks after background subtraction and peak deconvolution, due to the proximity of the signals of interest.

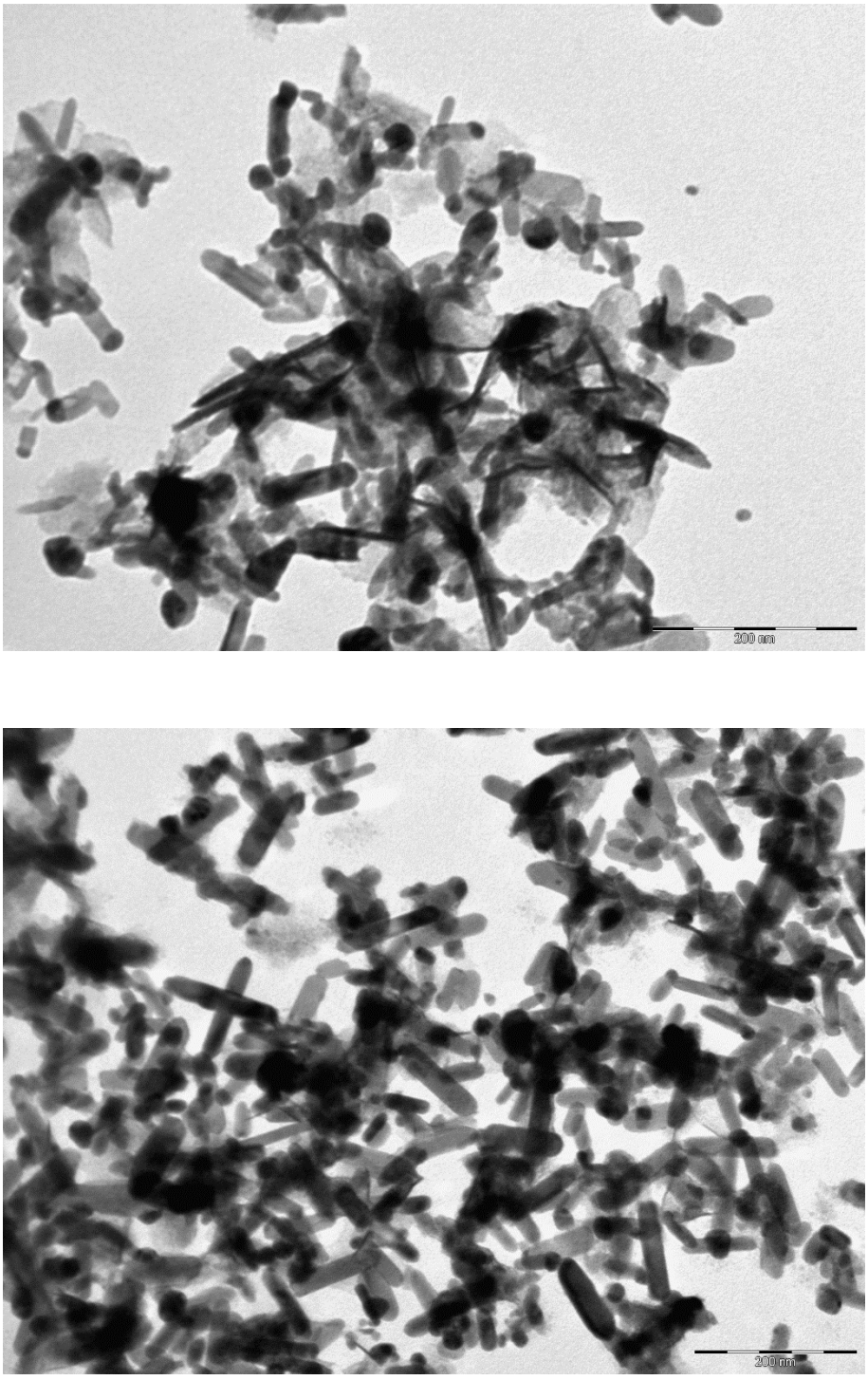

Figure S6. BF-TEM images representative of the reaction product after a reaction time of 15 min (top) and 60 min (bottom).

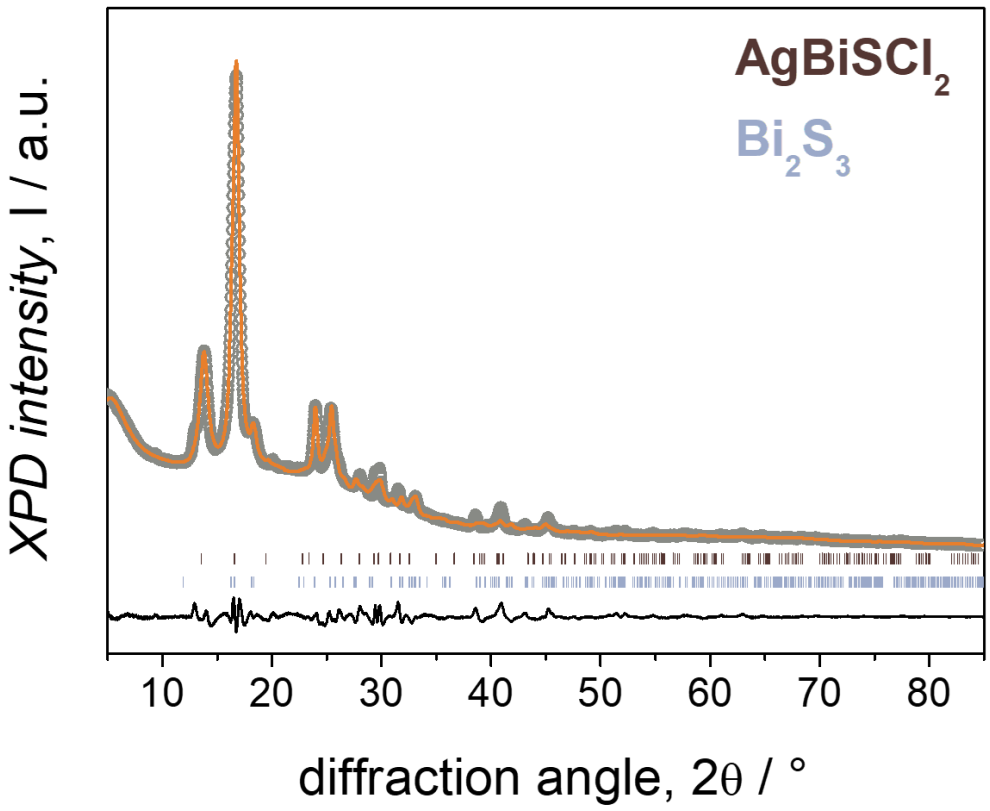

Figure S7. Rietveld refinement of the XRD pattern of the reaction product after a reaction time of 60 min, suggesting the presence of phases other than $AgBiSCl_2$.

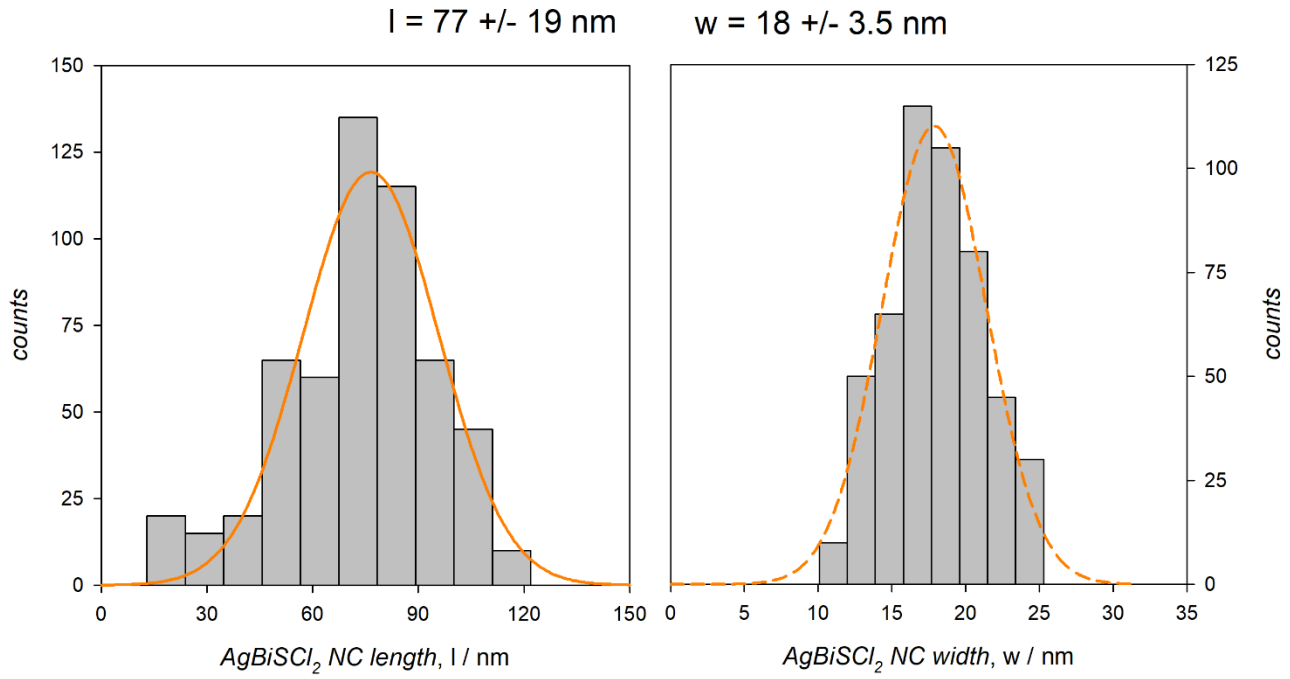

Figure S8. Distributions of lengths (left panel) and widths (right panel) of the colloidal $AgBiSCl_2$ NCs.

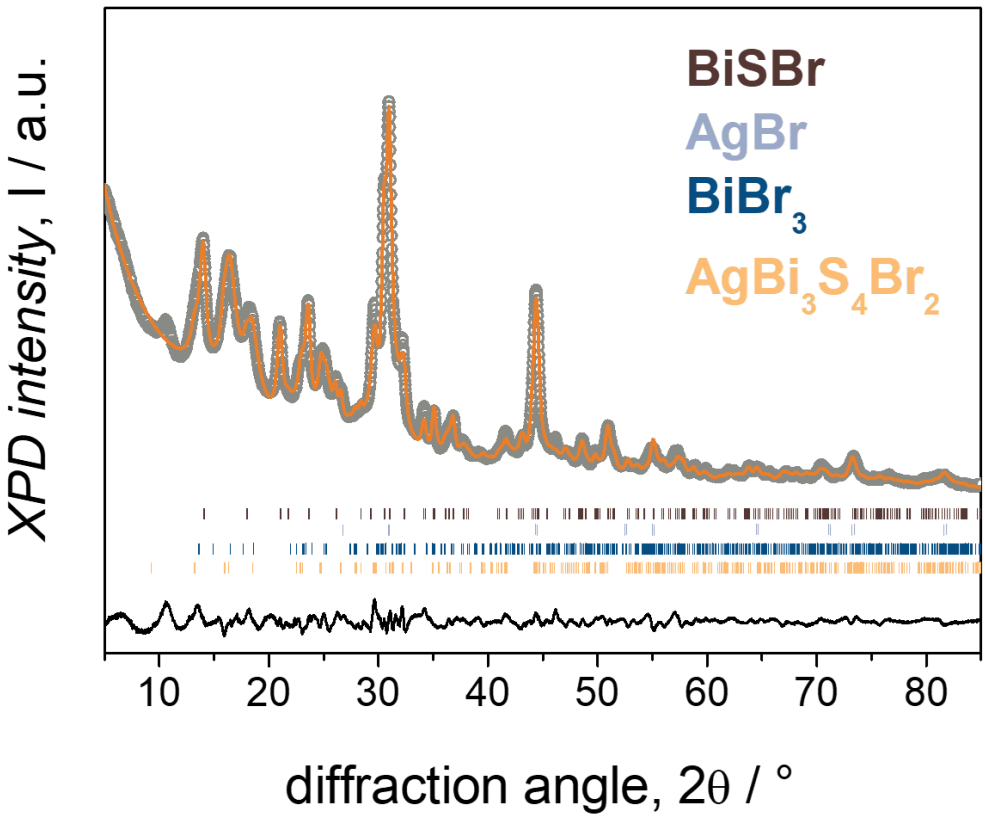

Figure S9. Rietveld refinement of the XRD pattern of the reaction product obtained upon attempting the synthesis of NCs of $AgBiSBr_2$.

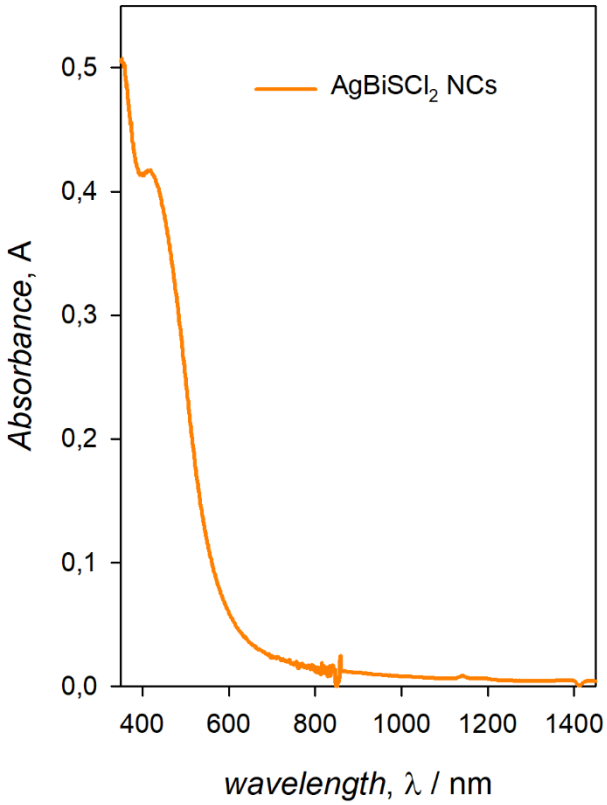

Figure S10. Absorption spectrum of a tetrachloroethylene dispersion of the colloidal $AgBiSCl_2$ NCs.

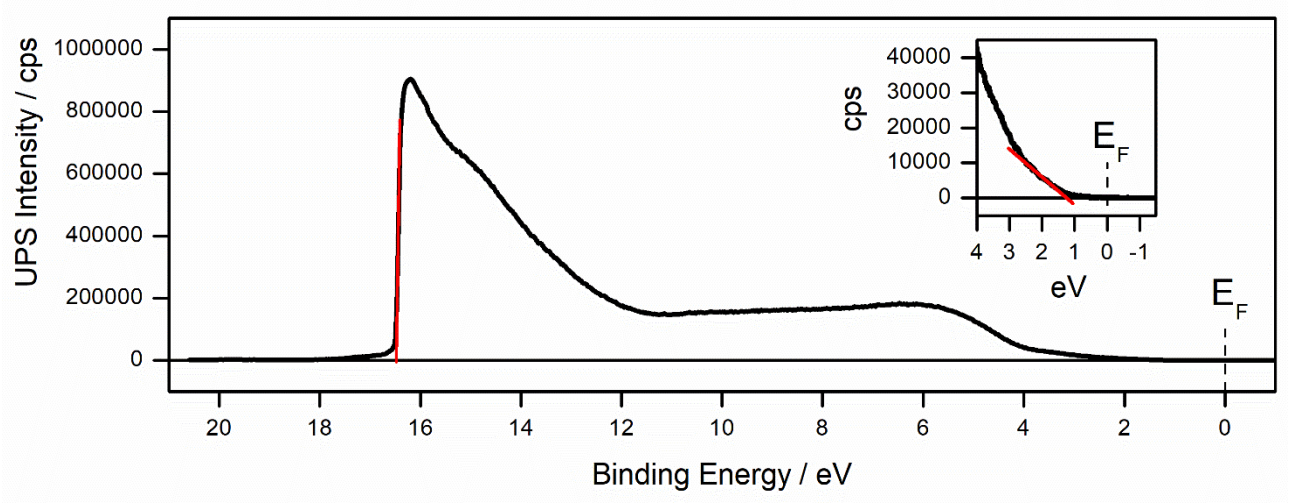

Figure S11. UPS spectrum of a solid film of the colloidal $AgBiSCl_2$ NCs.

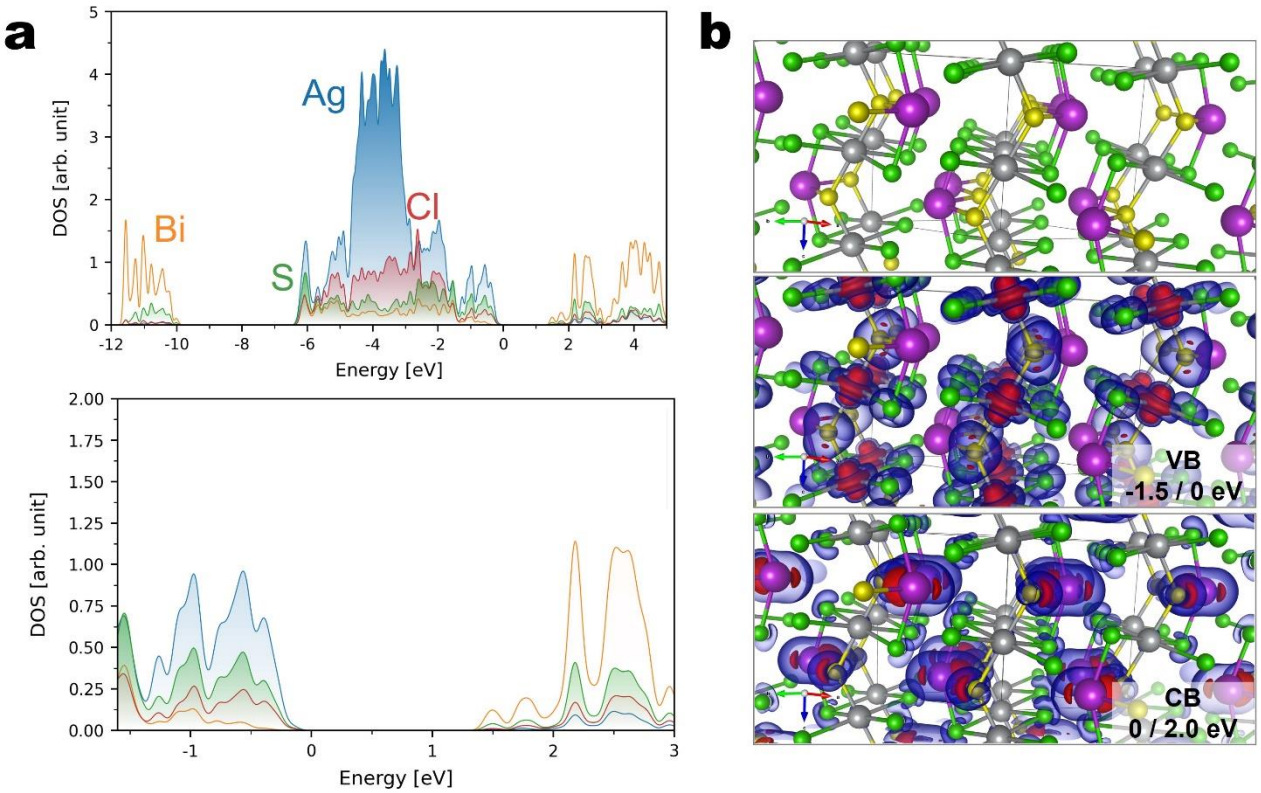

Figure S12. Density of states (DOS) and partial charge density of $AgBiSCl_2$. The DOS (a) is shown as atomic projections. The bottom panel shows an enlargement near the Fermi level. The partial charge density (b) is reported as isosurfaces for the valence band (VB) maximum (from -1.5 eV to the Fermi level, middle panel) and for the conduction band (CB) minimum (from Fermi level to +2.0 eV, bottom panel). The adopted isovalues are: 0.002 (blue) and 0.012 (red) for the VB and 0.0003 (blue) and 0.001 (red) for the CB, in VASP units. The top panel shows the same atoms as the VB and CB charge density images without isosurfaces, for clarity. Atom colors: Ag=grey, Bi=violet, Cl=green, S=yellow.

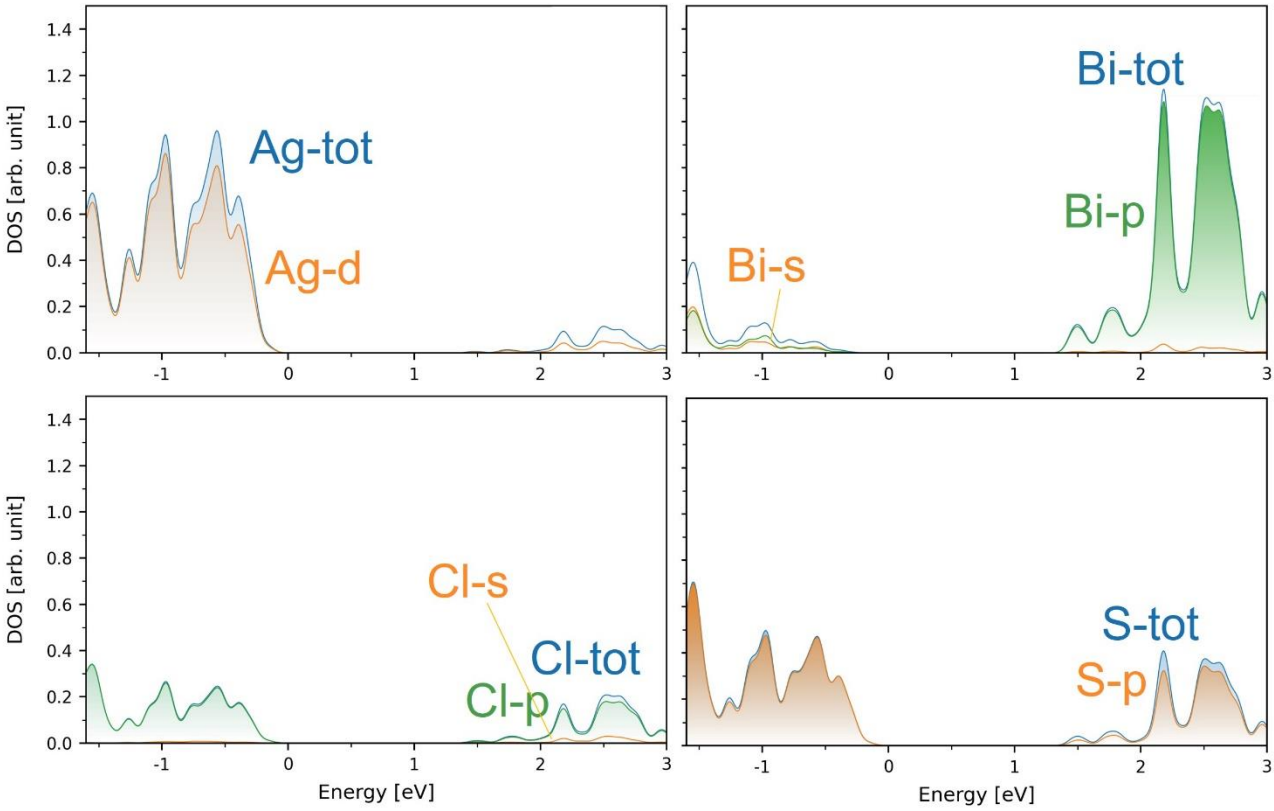

Figure S13. Density of states (DOS) projection onto atomic orbitals near the Fermi level. Each panel shows one atom type and the relative orbital decomposition. Orbital projections which give a negligible contribution to the DOS are not shown.

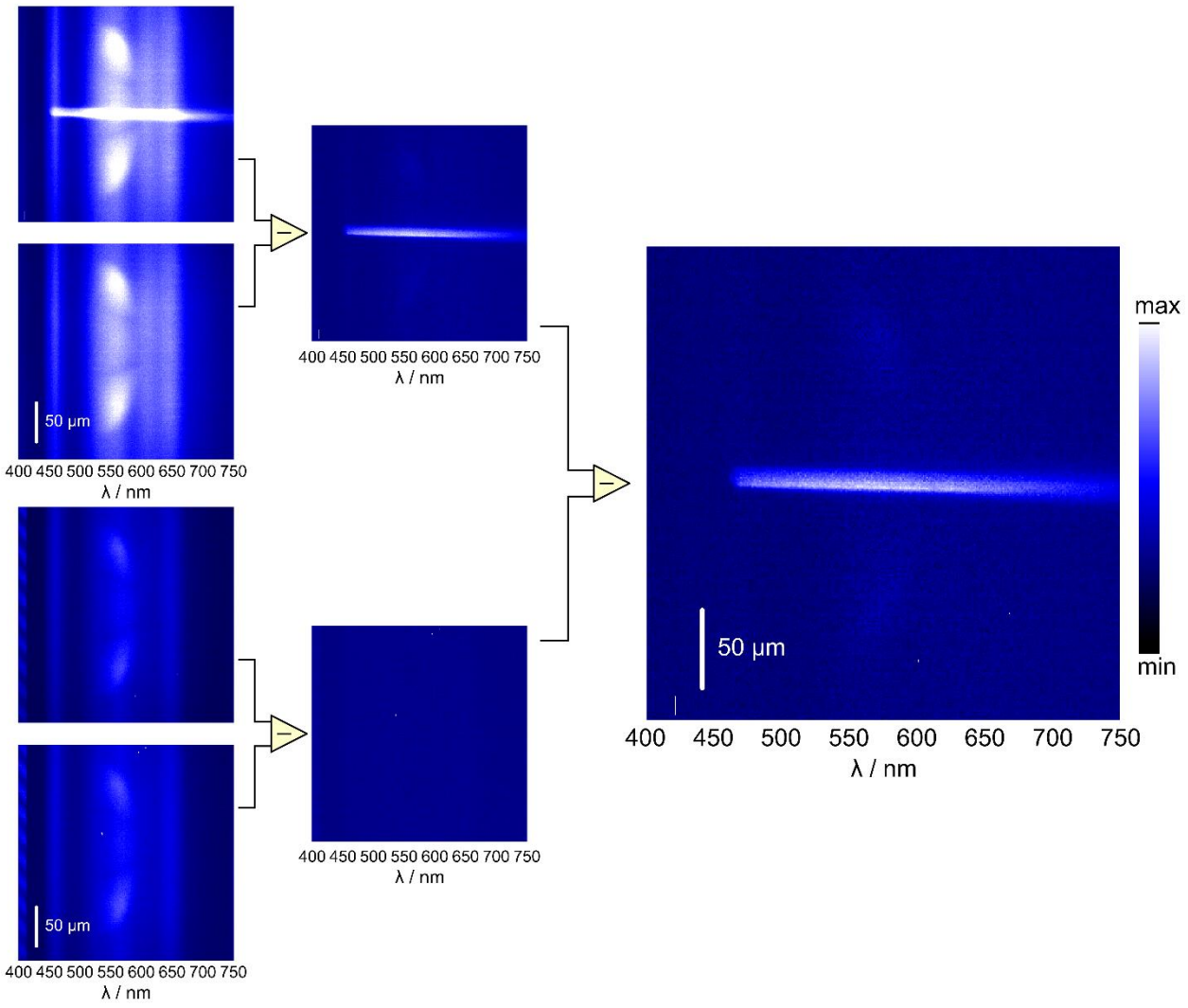

Figure S14. The final PL map of a $AgBiSCl_2$ NC film (large panel on the right side of the figure) resulted from the subtraction of the background (detected ambient light); to these data, the contribution of the bare substrate (minus its background) was further subtracted. In this representative case, also shown as Figure 5c, the temperature is 298 K and the fluence is 0.60 mJ/cm^2 (excitation at 400 nm; long pass filter at 450 nm).

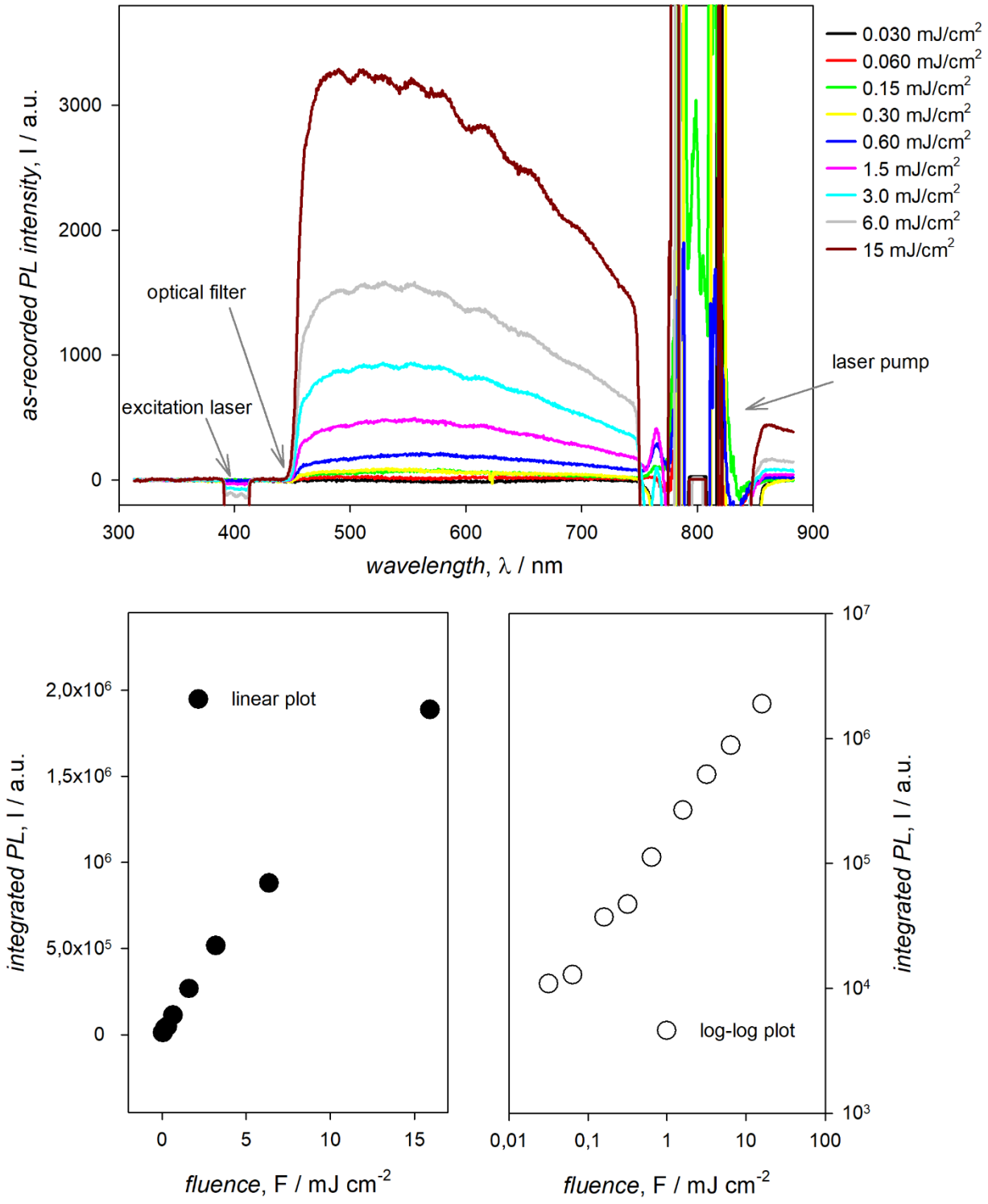

Figure S15. Fluence dependence (in between 15 μJ/cm^2 and 15 mJ/cm^2) of the PL of a $AgBiSCl_2$ NC film at room temperature (the fundamental laser pump at 800 nm was doubled by a BBO crystal to excite the NC film at 400 nm, which was cut by a long pass filter at 450 nm); the PL was integrated between 450 and 750 nm.

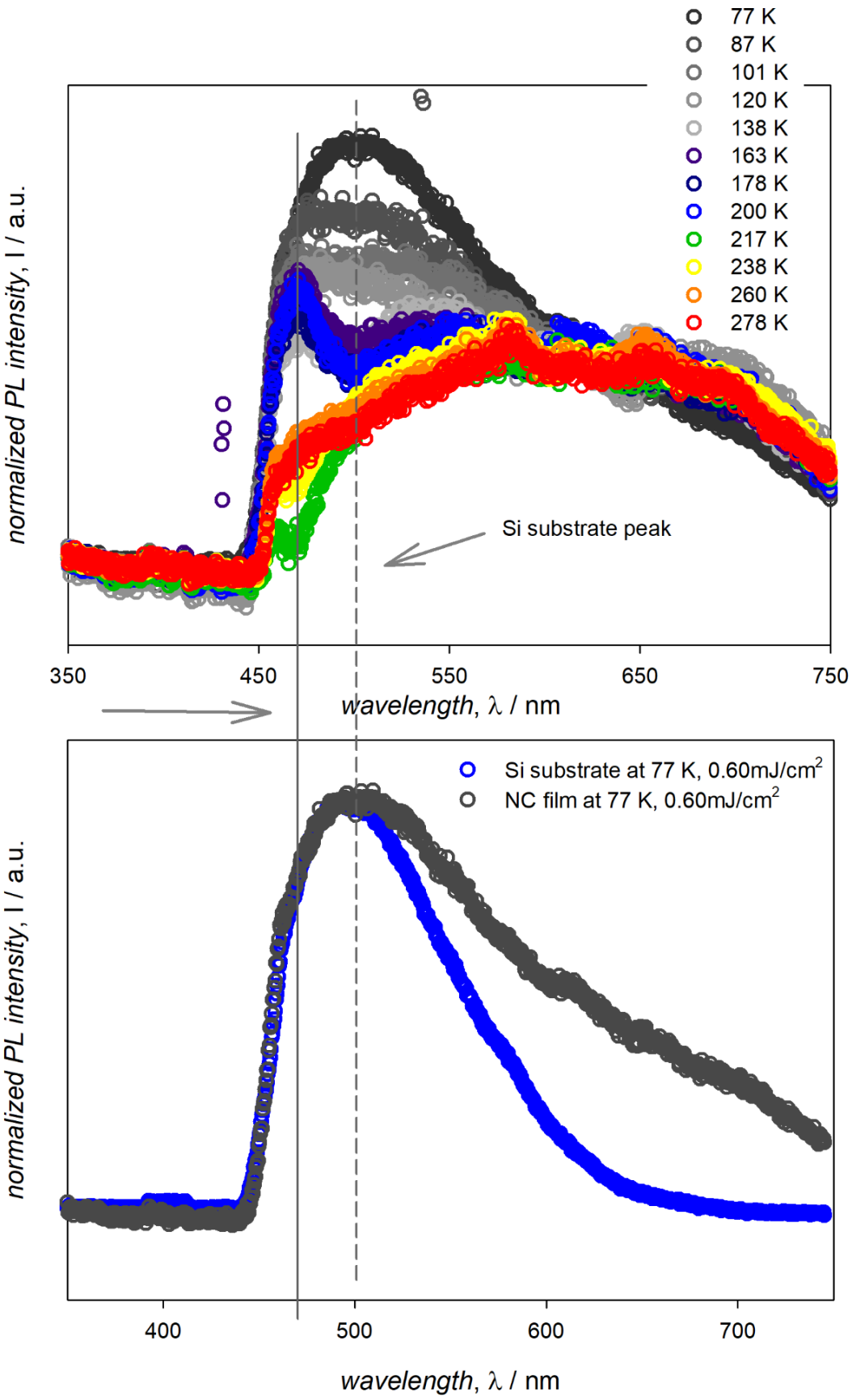

Figure S16. Temperature dependence of the PL of a $AgBiSCl_2$ NC film excited at 400 nm, 0.60 mJ/cm^2; data below 160 K are affected by the Si substrate, as highlighted in the lower panel comparing normalized PL at 77 K of the NC film and the bare Si substrate.

Supporting References.

S1. Altomare, A.; Corriero, N.; Cuocci, C.; Falcicchio, A.; Moliterni, A.; Rizzi, R. QUALX2.0: a qualitative phase analysis software using the freely available database POW_COD. *J. Appl. Cryst.* **2015**, *48*, 598.

S2. Gražulis, S.; Daškevič, A.; Merkys, A.; Chateigner, D.; Lutterotti, L.; Quirós, M.; Serebryanaya, N. R.; Moeck, P.; Downs, R. T.; Le Bail, A. Crystallography Open Database (COD): an open-access collection of crystal structures and platform for world-wide collaboration. *Nucleid Acids Research* **2012**, *40*, D420.

S3 Ruck, M.; Poudeu Poudeu, P. F.; Söhnel, T. Synthesis, Crystal Structure and Electronic Band Structure of the Isostructural Sulfide Chlorides $CuBiSCl_2$ and $AgBiSCl_2$. *Z. Anorg. Allg. Chem.* **2004**, *630*, 63.

S4. Altomare, A.; Cuocci, C.; Giacovazzo, C.; Moliterni, A.; Rizzi, R.; Corriero, N.; Falcicchio, A. EXPO2013: A kit of tools for phasing crystal structures from powder data. *J. Appl. Cryst.* **2013**, *46*, 1231.

S5. Altomare, A.; Campi, G.; Cuocci, C.; Eriksson, L.; Giacovazzo, C.; Moliterni, A.; Rizzi, R.; Werner, P. E. Advances in Powder Diffraction Pattern Indexing: N-TREOR09. *J. Appl. Cryst.* **2009**, *42*, 768.

S6. de Wolff, P. M. A Simplified Criterion for the Reliability of a Powder Pattern Indexing. *J. Appl. Cryst.* **1968**, *1*, 108.

S7. Altomare, A.; Caliandro, R.; Camalli, M.; Cuocci, C.; Da Silva, I.; Giacovazzo, C.; Moliterni, A. G. G, A. G.; Spagna, R. Space-Group Determination from Powder Diffraction Data: A Probabilistic Approach. *J. Appl. Cryst.* **2004**, *37*, 957.

S8. Giacovazzo, C. Phasing in Crystallography: A Modern Perspective. 2013, International Union of Crystallography/Oxford University Press.

S9. Rietveld, H. M. A profile refinement method for nuclear and magnetic structures. *J. Appl. Cryst.* **1969**, *2*, 65.

S10. Rodríguez-Carvajal, J. Recent advances in magnetic structure determination by neutron powder diffraction. *Phys. B: Condensed Matter* **1993**, *192*, 55.

S11. Farrow, C. L.; Juhás, P.; Liu, J. W.; Bryndin, D.; Boz.in, E. S.; Bloch, J.; Proffen, T.; Billinge, S. J. L. PDFfit2 and PDFgui: computer programs for studying nanostructure in crystals. *J. Phys.: Condens. Matter* **2007**, *19*, No. 335219.